Effects of Ti and Cr Additions in a Co–Ni–Al–Mo–Nb-Based Superalloy

Nithin Baler, Prafull Pandey, Mahendra Pratap Singh, Surendra Kumar Makineni, and Kamanio Chattopadhyay

Abstract

In the present work, we show the feasibility of microstructural control by additions of Ti and Cr to a γ/γ' Co-30Ni–10Al–5Mo–2Nb superalloy. Solutioning at 1300 °C followed by aging at 900 °C leads to homogenous distribution of $L1_2$ ordered cuboidal γ' precipitates in face-centered-cubic (fcc) γ matrix. Compositional measurements show Al, Mo, and Nb partition to γ' that indicates the γ' can be described as $(Co, Ni)_3(Al, Mo, Nb)$. An addition of 2 at.% Ti leads to increases in the γ' volume fraction from 56% to 70% and solvus temperature from 990 °C to 1030 °C. Ti strongly partitions to γ' with respect to γ matrix. Similarly, an addition of 10 at.% Cr to the base alloy leads to a morphological transition of γ' precipitates from cuboidal to near spherical shape, indicating a direct influence on the γ/γ' lattice misfit. Unlike Ti, Cr partitions to γ matrix, and additionally, Cr influences Mo to partition into γ matrix. A combined addition of Ti and Cr leads to high γ' volume fraction ~76% and an increase in γ' solvus temperature to 1045 °C, while maintaining the spherical γ' morphology. These superalloys show 0.2% proof strength comparable to those of Co–Al–W-based superalloys. At 870 °C, 10 at.% Cr and 2 at.% Ti added alloys show higher specific 0.2% proof stress than Co–Al–W-based superalloys. The obtained results show the microstructural sensitivity of these Co-based superalloys toward their designing for better performance.

Keywords

Cobalt-based superalloys • Microstructure • γ' morphology • γ' volume fraction • Electron microscopy • Energy dispersive spectroscopy (EDS)

Introduction

Design of γ/γ' superalloys with combined hot-corrosion resistance and high temperature strength is still a major technological goal for material scientists. These superalloys are mainly utilized in fabricating critical parts in hot section of turbine engines (both aero-based or land-based) where the temperature reaches up to 1600 °C [1]. The major fraction of these superalloys that are commercially used are Ni-based. Recent work showed that Co-based γ/γ' superalloys might be the possible alternatives to Ni-based alloys with better resistance to high temperature environmental degradation and comparable mechanical properties [2–4]. The conventional Co-based alloys are solid solution/carbide strengthened, and their applications were limited by their inferior high temperature strength in comparison to the γ/γ' Ni-based superalloys that are used with expensive thermal barrier coatings [5, 6].

Among these γ/γ' Co-based superalloys, Co–Al–W system is the most explored in the last decade for making them suitable in several high temperature applications [7–14]. Here, the strengthening γ' phase is $Co_3(Al, W)$ which is a metastable phase with $L1_2$ ordered crystal structure coherently embedded in face-centered-cubic (fcc) γ-Co matrix. Several alloying additions, such as Ni, Cr, Ti, Ta, Nb, Hf, B, etc., were carried out to improve the γ/γ' microstructural stability and strengthening ability at temperatures beyond 1000 °C aiming to exceed those of Ni-based superalloys [15–18]. In particular, Ni, Ti, and Ta increase the volume fraction of strengthening γ' phase and γ' solvus temperature while Cr significantly improves the high temperature

N. Baler · P. Pandey · M. P. Singh · S. K. Makineni (✉) · K. Chattopadhyay
Department of Materials Engineering, Indian Institute of Science, (SKM), Bangalore, 560012, India
e-mail: skmakineni@iisc.ac.in

S. Tin et al. (eds.), *Superalloys 2020*, The Minerals, Metals & Materials Series,
https://doi.org/10.1007/978-3-030-51834-9_91

oxidation resistance [19, 20]. However, the major concern with these alloys are their high mass densities (>9.2 g/cm^3) due to the need of adding high amount of W (~25 wt%) for stabilizing γ/γ' microstructure. This can impose a restriction on their applications where the strength to weight ratio is very critical.

In 2015, alloys based on Co–Al–Mo–Nb/Ta system were shown to exhibit metastable γ/γ' microstructure similar to Co–Al–W-based and Ni-based superalloys [21–24]. In comparison, these alloys have much lower mass densities (8.2–8.6 g/cm^3) and some of the optimized compositions with Ni additions show higher yield strength than Co–Al–W–based superalloys at temperatures above 800 °C. Considering present knowledge on the alloying behavior, the present work describes the effect of Ti and Cr on Co–Ni–Al–Mo–Nb-based superalloy. The two main factors responsible for the high temperature capability and strength are the solvus temperature and the microstructure. In this work, we demonstrated that these factors can be controlled by additions of Ti and Cr. Further, high temperature mechanical properties were evaluated and compared with the existing Co-based superalloys.

Experimental

A laboratory scale vacuum arc melting unit was used to prepare alloys with nominal compositions Co–30Ni–10Al–5Mo–2Nb (2Nb), Co–30Ni–10Cr–10Al–5Mo–2Nb (2Nb10Cr), Co–30Ni–10Al–5Mo–2Nb–2Ti (2Nb2Ti), and Co–30Ni–10Cr–10Al–5Mo–2Nb–2Ti (2Nb10Cr2Ti) (all in at.%) under an argon atmosphere in the form of 30 g ingots in a water cooled copper hearth. Subsequently, these were cast into 3 mm rods using a vacuum arc suction casting unit equipped with water cooled split copper mold. The rods were solutionized at 1300 °C for 15 h under vacuum (10^{-6} mbar) followed by quenching in water. Sample was cut from the solutionized rods and sealed in quartz tube under a vacuum of 10^{-5} mbar. The sealed samples were then aged at 900 °C for 50 h in a box furnace and subsequently furnace cooled.

For transmission electron microscopy (TEM), samples were cut in the form of 3 mm disks with a thickness of approximately 0.8 mm from the aged samples and mechanically polished to a thickness of about 80 µm. These samples were made electron transparent by fine polishing using a precision ion polishing system (PIPS, GATAN^{TM}). The microstructure of the aged alloys was investigated using a TEM (F30, FEI) equipped with a field emission gun. The compositions of the phases in the alloy microstructures were measured using X-ray energy dispersive spectroscopy (EDS) attached to the microscope in a scanning-TEM (STEM) nanoprobe mode. The partition coefficients (K_i) were calculated for an element i between the γ/γ' phases by the formula:

$$K_i = C_i^{\gamma'} / C_i^{\gamma}$$

where $C_i^{\gamma'}$ and C_i^{γ} are the concentration of constituent element i in γ' and γ phases, respectively.

The γ' solvus temperature of the aged alloys was determined by heating at a rate of 10 °C/min in a differential scanning calorimeter (DSC) operated under an argon atmosphere. The 0.2% yield strength of the aged alloys was measured by compression tests using a DARTEC hydraulic machine operated with a strain rate of 10^{-3} s^{-1} at temperatures up to 870 °C. The mass density of the alloys was measured in accordance with the ASTM standard B311-08 at room temperature while the volume fraction of γ' precipitates for the aged alloys was estimated using ASTM standard E562-11.

Results and Discussion

Microstructure of Aged 2Nb Superalloy

Figure 1 shows microstructural analysis of 2Nb superalloy after aging at 900 °C for 50 h. The selected area electron diffraction pattern (SAEDP), inset of Fig. 1a, taken along [100] zone axis reveals the appearance of superlattice spots corresponding to $L1_2$ ordering along with the spots of fcc γ matrix. The darkfield image taken using 001 superlattice spot shows cuboidal γ' precipitates in the γ matrix as shown in Fig. 1a.

The size of γ' precipitates ranges between 250 and 300 nm with a γ' volume fraction of 56% in the alloy. Figure 1b shows high angle annular darkfield (HAADF) STEM image of a similar region from the aged alloy showing Z-contrast (atomic number contrast) across the γ and γ' precipitates. Figure 1c shows EDS elemental maps across a few γ' precipitates, indicating partitioning of the constitute elements across the two phases. Al and Nb show strong partitioning to the γ' with respect to γ matrix while Mo shows weak partitioning to the γ'. Figure 1d shows the compositional line profiles across a few γ' precipitates and Table 1 shows the measured compositions of γ and γ' along with the calculated partitioning coefficients (K_i) of the constituent elements. We observe K_{Al} and K_{Nb} are much greater than 1 while K_{Mo} is slightly greater than 1. The total content of Al, Mo, and Nb in the γ' is found to be approximately 21 at.% that suggests the $L1_2$ γ' precipitates can be described as $(Co, Ni)_3(Al, Mo, Nb)$ with Al, Mo, and Nb occupying the {0,0,0} positions in its $L1_2$ unit cell.

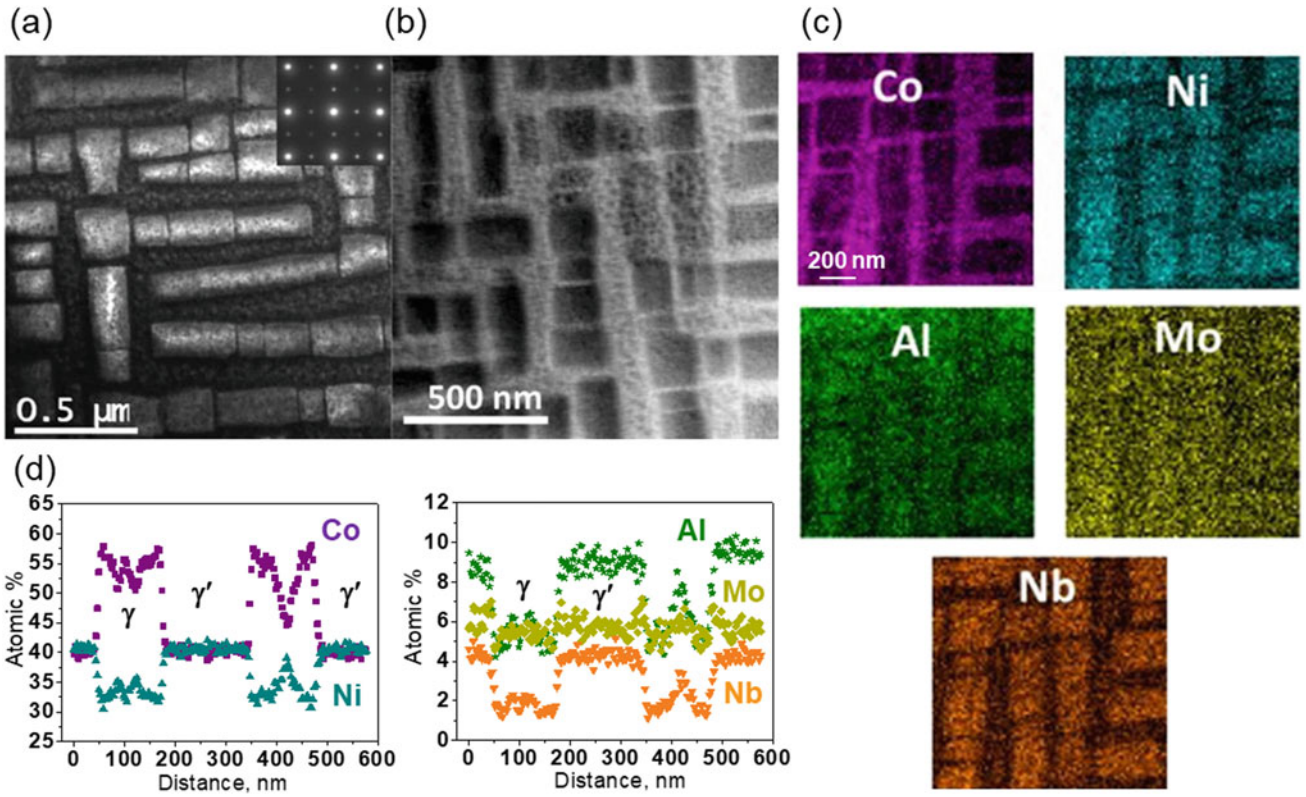

Fig. 1 **a** Darkfield micrograph taken using 001 superlattice spot near to [100] fcc matrix zone axis for 2Nb superalloy after aging at 900 °C for 50 h. The diffraction pattern is shown as an inset. **b** HAADF STEM image from a region containing a few γ' precipitates. **c** EDS elemental maps of a few γ' precipitates and **d** compositional line profiles across γ' precipitates using STEM nanoprobe

Table 1 Comparison of compositions of γ and γ' in 2Nb, 2Nb2Ti, 2Nb10Cr, and 2Nb10Cr2Ti alloys (all in at.%)

	2Nb			2Nb2Ti			2Nb10Cr			2Nb10Cr2Ti		
	γ	γ'	K_i	γ	γ'	K_i	γ	γ'	K_i	γ	γ'	K_i
Co	55.9	40.3	0.7	55.4	40.1	0.7	40.9	31.9	0.8	41.3	32.8	0.8
Ni	32.9	39.1	1.2	33.4	36.3	1.1	31.9	41.7	1.3	30.5	39.9	1.3
Cr							14.6	5.6	0.4	15.6	5.8	0.4
Al	6.1	11.6	1.9	5.9	11.2	1.9	6.1	13.3	2.2	5.7	10.9	1.9
Mo	4.5	5.8	1.3	4.9	5.4	1.1	6.3	4.4	0.7	6.5	4.6	0.7
Nb	0.4	3.6	8.0	0.5	3.8	7.6	0.4	3.1	7.8	0.3	2.9	9.7
Ti				0.5	3.2	6.4				0.4	3.1	7.8

Microstructure of Aged 2Nb2Ti Superalloy

Figure 2 shows the microstructural analysis results on the 2Nb2Ti superalloy after aging. The inset in Fig. 2a shows SAEDP taken along [100] zone axis from a region of the alloy. Like 2Nb alloy, it reveals γ' $L1_2$ superlattice spots along with the fcc γ matrix spots. The darkfield image taken from 100 superlattice spot reflects the cuboidal γ' precipitates in fcc γ matrix. There is no effect of 2 at.% Ti on the γ' morphology while the γ' volume fraction increases to 70%. Figure 2b shows the EDS elemental maps (Fig. 2c) from a region containing a few γ' precipitates, presenting strong partitioning of Ti to γ' with respect to γ matrix. Figure 2c shows the compositional line profiles across a few γ' precipitates. The measured compositions of γ and γ' phases along with the partitioning coefficients were tabulated in Table 1. There was no significant effect of Ti on the K_i values of other elements except Mo that tends to partition equally across γ and γ' precipitates. K_{Ti} was estimated to be larger than 6, indicating that Ti is a strong γ' stabilizer in the alloy. The total content sum of Al, Mo, Nb, and Ti suggests the $L1_2$ γ' phase can be described as $(Co, Ni)_3(Al, Mo, Nb, Ti)$ with Ti occupying the {0,0,0} positions along with Al, Mo, and Nb in the unit cell.

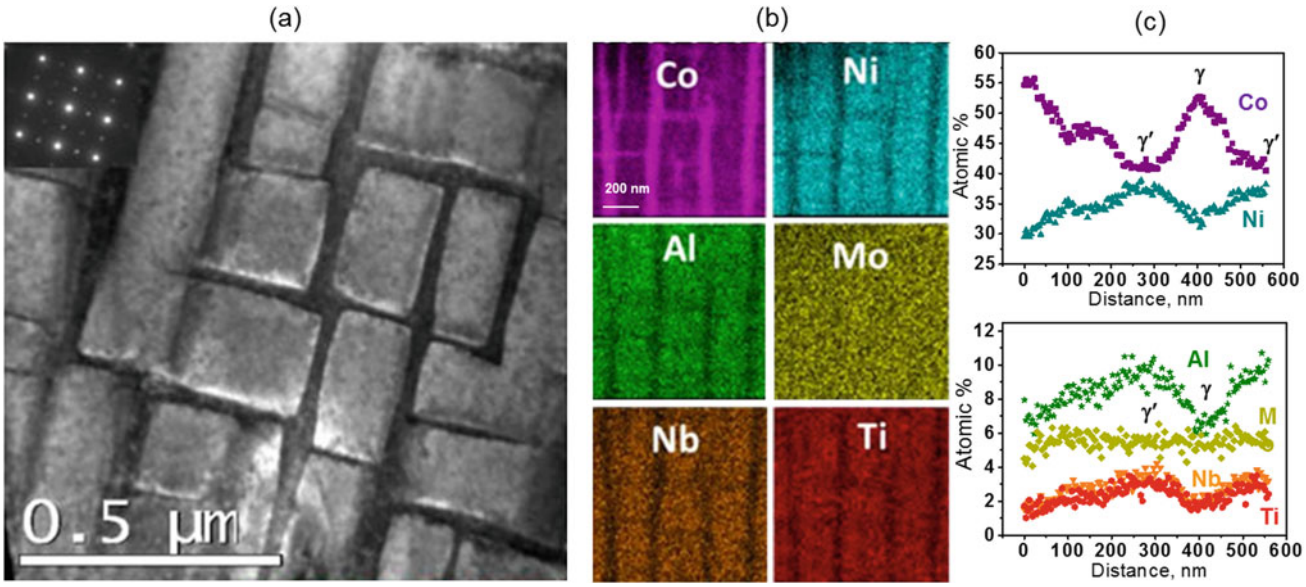

Fig. 2 **a** Darkfield micrograph taken using 001 superlattice spot near to [100] zone axis for 2Nb10Ti superalloy after aging at 900 °C for 50 h. The diffraction pattern is shown as an inset. **b** EDS elemental maps of a few γ' precipitates and **c** compositional line profiles across γ' precipitates using STEM nanoprobe

Microstructure of Aged 2Nb10Cr Superalloy

Figure 3 shows the microstructural analysis for 2Nb10Cr superalloy after aging. The inset in Fig. 3a shows a SAEDP taken along [100] zone axis that reveals $L1_2$ ordered superlattice spots along with the fcc γ matrix spots. The darkfield image taken from a 001 ordered spot reflects spherical γ' precipitates in γ matrix as shown in Fig. 3a. The diameter of the ordered γ' precipitates was in the range of 250–300 nm with γ' volume fraction of around 66%. Figure 3(b) shows EDS elemental maps taken from a region containing γ' precipitates, suggesting Cr partitions to γ matrix with respect to γ' precipitates.

Figure 3c shows the compositional line profiles across a γ' precipitate. The measured compositions of γ and γ' with the constituent element partitioning coefficients (K_i) are shown in Table 1. K_{Cr} was found to be less than 1 and no significant change in the K_i values for other elements was observed except for Mo. K_{Mo} becomes less than 1 as compared to the base 2Nb superalloy. These results show that an addition of Cr led to the change in γ' morphology from cuboidal to spherical shape.

Microstructure of Aged 2Nb10Cr2Ti Superalloy

Figure 4 shows microstructural analysis results on 2Nb10Cr2Ti superalloy after aging. Figure 4a shows HAADF STEM image that reveals the γ' precipitates are spherical and interconnected/coagulated with very lower inter-particle distance compared to 2Nb10Cr superalloy. Addition of 2 at.% Ti increases the volume fraction of γ' precipitates to around 76%. Figure 4b and c shows EDS elemental maps from a region containing a γ' precipitate and the compositional line profiles indicate the partitioning behavior of other elements remain unaffected as compared to 2Nb10Cr superalloy. The measured compositions of γ and γ' are shown in Table 1. Ti shows strong partitioning ($K_{Ti} > 7$) to γ' with respect to γ matrix. Like 2Nb10Cr, K_{Mo} and K_{Cr} was found to be smaller than 1.

Physical and Mechanical Properties

Figure 5a shows a comparison of γ' solvus temperature of the four alloys examined. An addition of 2 at.% Ti in 2Nb2Ti superalloy led to an increase in the solvus temperature by 40 °C as compared to the base 2Nb superalloy having 990 °C. An addition of 10 at.% Cr also increased the solvus temperature by 15 °C. The combined addition of 2 at.% Ti and 10 at.% Cr increased the solvus temperature by 55–1045 °C.

Figure 5b shows the comparison of mass densities of the four alloys with other Co-based superalloys. The base 2Nb superalloy has a density of 8.38 g/cm^3. On addition of Ti and/or Cr, the mass densities were lowered up to 8.24 g/cm^3. These values are lower than the other commercial Co-based alloys and Co–Al–W-based superalloys [8].

Figure 5c shows a plot of the compressive 0.2% proof stress as a function of temperature comparing the present

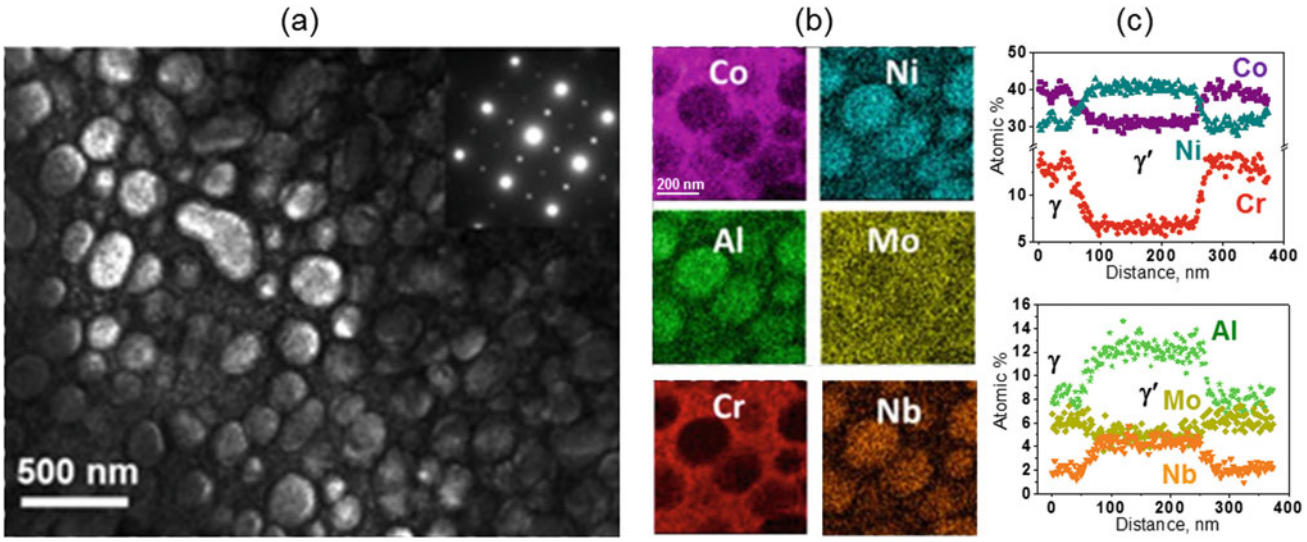

Fig. 3 **a** Darkfield micrograph taken using 001 superlattice spot near to [100] zone axis for 2Nb10Cr superalloy after aging at 900 °C for 50 h. The diffraction pattern is shown as an inset. **b** EDS elemental maps of a few γ' precipitates and **d** compositional line profiles across a γ' precipitate using STEM nanoprobe

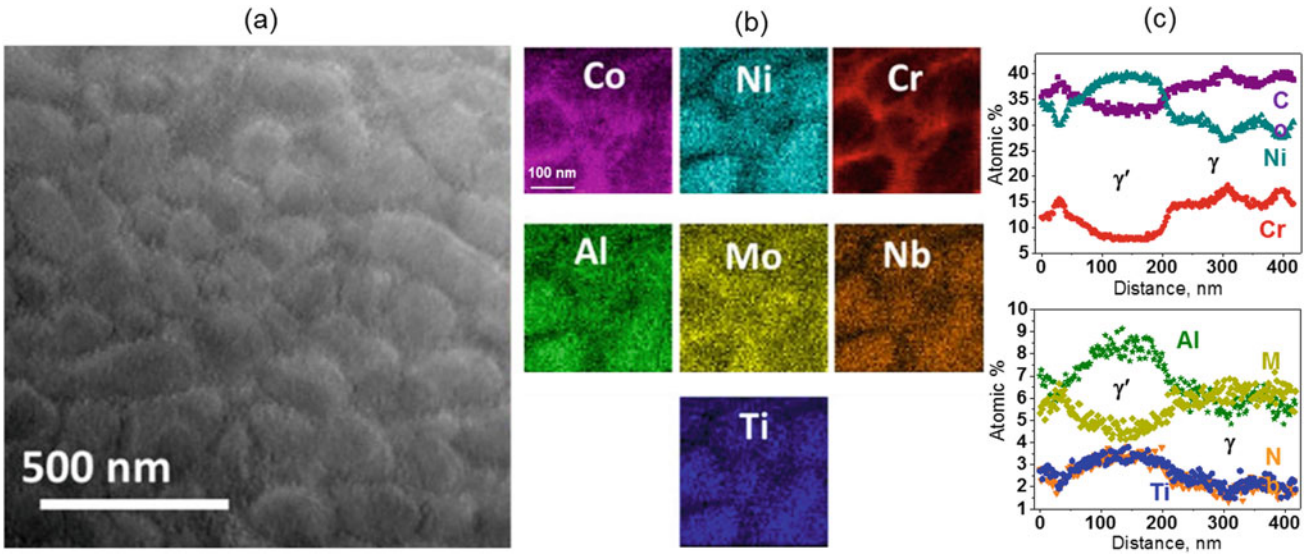

Fig. 4 **a** HAADF STEM image for 2Nb10Cr2Ti alloy after aging at 900 °C for 50 h**b** EDS elemental maps of a few γ' precipitates and **c** compositional line profiles across a γ' precipitate using STEM nanoprobe

alloys and other Co-based superalloys. At room temperature, 2Nb, 2Nb10Cr, and 2Nb2Ti alloys show comparable 0.2% proof stress values ($\sim$735 MPa), which is higher than those of Co-9.4Al-11 W and Co-8.8Al-9.8 W-2Ta alloys [8]. At 870 °C, 2Nb10Cr and 2Nb2Ti show 0.2% proof stress of 500 and 535 MPa, respectively, that are higher than those of other Co-based superalloys except Co-8.8Al-9.8 W-2Ta alloy. However, these two alloys have higher specific 0.2% proof stress (Fig. 2d) than Co-8.8Al-9.8 W-2Ta alloy at 870 °C.

Discussion

The above experimental results show the effects of Ti and Cr additions on the γ/γ' microstructure of Co-30Ni-10Al-5Mo-2Nb superalloy (2Nb). Addition of 2 at.% Ti to 2Nb and 2Nb10Cr led to increases in the both γ' volume fraction and γ' solvus temperature (Figs. 5a and 6a for comparison). The partitioning of Ti ($K_{Ti} > 6$) to γ' precipitates with respect to γ matrix phase shows that Ti is a strong γ' stabilizer

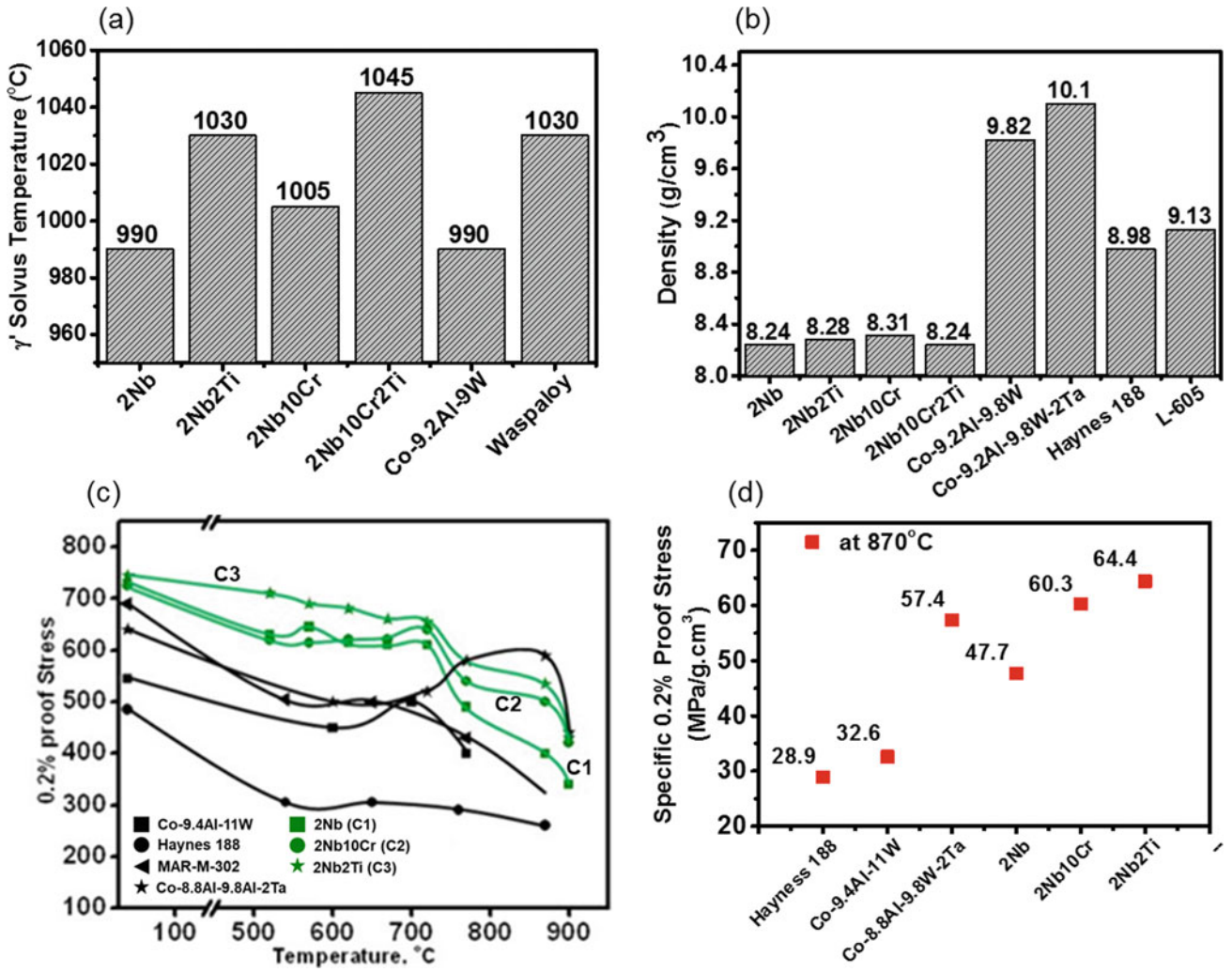

Fig. 5 **a** Comparison of γ' solvus temperature and **b** mass densities of 2Nb, 2Nb2Ti, 2Nb10Cr, and 2Nb10Cr2Ti superalloys with other Co-based superalloys, **c** Comparison of 0.2% proof stress versus temperature and **d** specific 0.2% proof stress values at 870 °C for 2Nb, 2Nb2Ti, and 2Nb10Cr superalloys with other Co-based superalloys

(see Fig. 6b for comparison of K_i values). In the binary Co–Ti phase diagram [25], a stable Co_3Ti phase exists with the $L1_2$ ordered structure. Thus, it is expected that Ti stabilizes $L1_2$ ordering of γ' by partitioning into it. Similar $L1_2$ structural stabilizing effect was seen on Ti addition to Co–Al–W-based and Co–Ni–Al–Mo–Ta-based superalloys. First principle calculations revealed that Ti substitution in $L1_2$ $Co_3(Al, W)$ results in a reduction in its formation energy by lowering the binding energy between Ti and their nearest neighbors in the ordered unit cell [26]. Omori et al. [27] showed the association between the elemental partitioning coefficients (K_i), formation enthalpy (ΔH^f), and solvus temperature for Co_3X (X = alloying addition) in $L1_2$ ordered structure. The calculations revealed a larger K_i value possesses more negative ΔH^f with a capability of increasing solvus temperature by higher degrees. Similarly, in $(Co, Ni)_3(Al, Mo, Ta)$ $L1_2$ compound [23], Ti substitution in Al sites results in a more negative ΔH^f value indicating the enhancement of its phase stability. More specifically, it was shown from the density of states (DOS) plots that the pseudo-gap deepens, and the Fermi level shifts toward the pseudo-gap after Ti substitution for Al sites. Hence, the γ' solvus temperature increases by roughly 50 °C by 2 at.% Ti addition in Co-30Ni-10Al-5Mo-2Ta superalloy [23]. In the present case, we observe an increment of approximately 40 °C by 2 at.% Ti addition in 2Nb superalloy. The increase in the γ' volume fraction can be related to the nature of the phase boundary between γ and γ' phases that is directly influenced by the solvus temperature. More specifically, higher γ' solvus temperature indicates steeper γ/γ' phase boundary, and thus, the solute supersaturation increases in the γ matrix at a specific temperature. Hence, during aging at

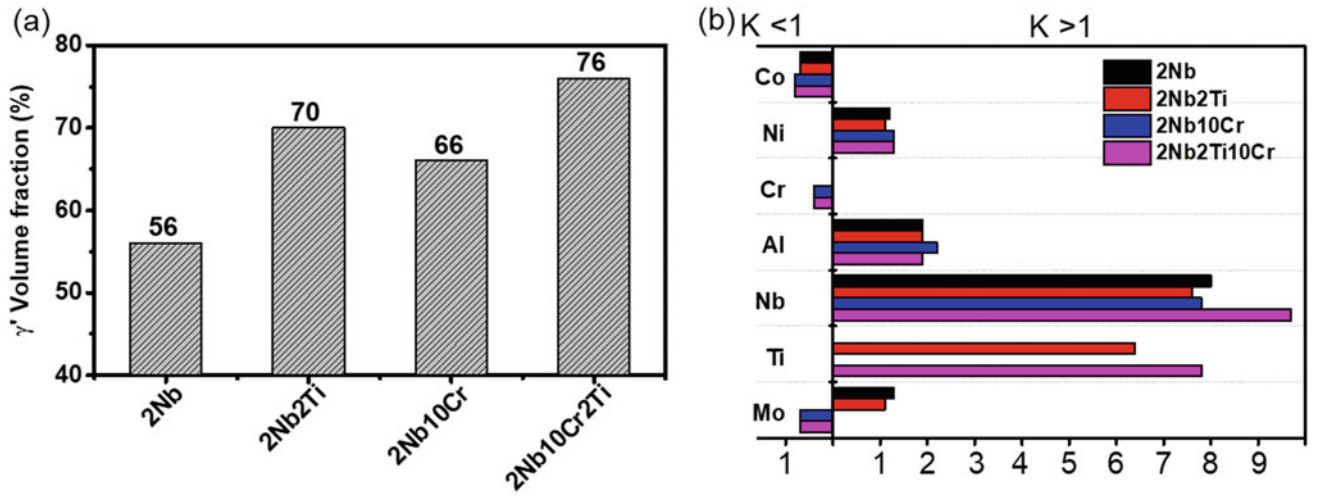

Fig. 6 **a** Comparison of γ' volume fraction and **b** elemental partitioning coefficients (K_i) for 2Nb, 2Nb2Ti, 2Nb10Cr, and 2Nb10Cr2Ti superalloys

900 °C, 2Nb2Ti and 2Nb10Cr2Ti alloys exhibit γ' volume fractions up to 76% compared to lower values for the base 2Nb alloy (56%).

An addition of 10 at.% Cr transforms γ' morphology from cuboidal to spherical as shown for the 2Nb10Cr and 2Nb10Cr2Ti alloys. Additionally, we also observe an increment in the γ' solvus temperature by approximately 15 °C compared to 2Nb and 2Nb2Ti alloys, which is not the case in Co–Al–W-based superalloys where the γ' solvus decreases with Cr addition. The spherical morphology of the γ' precipitates can be attributed to the reduction of γ/γ' lattice misfit toward close to zero. This misfit reduction causes a decrease in strain energy contribution to the total free energy, and thus, the domination of interfacial energy contribution occurs. This results in the system to choose spherical morphology of the γ' precipitates embedded in γ matrix phase. Similar microstructural transition effects were seen on the addition of varying amount of Cr up to 8 at.% in Co–30Ni–10Al–5Mo–2Ta superalloys [28, 29]. It was shown that the site occupancy behavior of Cr in the γ' $L1_2$ unit cell governs the γ/γ' lattice misfit. More specifically, with increasing the Cr content in the alloy, the Cr atoms changes preference of site occupation. That is up to 5 at.% Cr in the alloy, it prefers to replace Mo and anti-site Co atoms from the B-sites ({0,0,0} lattice positions) while at higher Cr composition, it also replaces Co atoms from A-sites. This led to the decrease in K_{Mo} values from 1.24 to 0.78, i.e., Mo partitions to γ matrix phase in Cr-containing alloys [29]. The replacement of larger size Mo atoms from the γ' precipitate to the γ matrix reduces the γ/γ' lattice misfit that was attributed to the γ' morphological transition from cuboidal to spherical shape in Cr-containing Co–30Ni–10Al–5Mo–2Ta superalloys. Similar effect of 10 at.% Cr addition to 2Nb and 2Nb2Ti alloys shows the change of K_{Mo} from greater than 1 to less than 1 that explains the observed spherical γ' precipitates in 2Nb10Cr and 2Nb10Cr2Ti alloys. It was also shown that at an optimum value of Cr composition in Co–30Ni–10Al–5Mo–2Ta alloy, the γ' formation enthalpy (ΔH^f) becomes more negative, and hence, the γ' solvus temperature increases by 39 °C for 5 at.% Cr-containing alloy [29]. In the 2Nb and 2Nb2Ti alloys, we observe, on addition of 10 at.% Cr, the increment in the γ' solvus temperature by 15 °C. Hence, we propose Cr induces the same effect of reducing the γ' formation enthalpy (ΔH^f) in the present alloys. Additionally, we also observe a slight increase in the γ' volume fraction in Cr-containing alloys that can be attributed to the steeper γ/γ' phase boundary due to increase in the γ' solvus temperature.

Hence, we can modulate or control the γ/γ' lattice misfit and the γ' volume fraction in the present Co–Ni–Al–Mo–Nb-based superalloys by additions of Ti and Cr that can also influence the high temperature coarsening kinetics of the γ' precipitates.

Conclusions

Additions of Ti and Cr to Co–Ni–Al–Mo–Nb superalloys have a significant effect on increasing the γ' solvus temperature (up to 1045 °C) and γ' volume fraction (up to 76%). Ti strongly partitions to γ' while Cr partitions to γ matrix. In Cr-containing alloys, partitioning preference of Mo changes from γ' to γ phase. This results in change of γ' morphology from cuboidal to spherical shape. 2Nb2Ti and 2Nb10Cr alloys show higher specific 0.2% proof stress values than Co–Al–W-based alloys.

References

1. Reed RC, Tao T, Warnken N (2009) Alloys-By-Design: Application to nickel-based single crystal superalloys. Acta Materialia 57:5898–5913. https://doi.org/10.1016/j.actamat.2009.08.018.
2. Suzuki A, DeNolf GC, Pollock TM (2007) Flow stress anomalies in γ/γ′ two-phase Co–Al–W-base alloys. Scripta Materialia 56:385–388. https://doi.org/10.1016/j.scriptamat.2006.10.039.
3. Suzuki A, Pollock TM (2008) High-temperature strength and deformation of γ/γ′ two-phase Co–Al–W-base alloys. Acta Materialia 56:1288–1297. https://doi.org/10.1016/j.actamat.2007.11.014.
4. Xue F, Zenk CH, Freund LP, Hoelzel M, Neumeier S, Göken M (2018) Double minimum creep in the rafting regime of a single-crystal Co-base superalloy. Scripta Materialia 142:129–132. https://doi.org/10.1016/j.scriptamat.2017.08.039.
5. Dardi LE, Shankar S (1986) Superalloy coating composition with oxidation and/or sulfidation resistance. US. patent US4615864A, 7 October 1986.
6. Antony KC (1983) Wear-resistant cobalt-base alloys. JOM 35:52–60. https://doi.org/10.1007/bf03338205.
7. Lee CS (1971) Precipitation-hardening characteristics of ternary cobalt-aluminum-X alloys, Ph.D. thesis, University of Arizona.
8. Sato J, Omori T, Oikawa K, Ohnuma I, Kainuma R, Ishida K (2006) Cobalt-base high-temperature alloys. Science 312:90–91. https://doi.org/10.1126/science.1121738.
9. Shinagawa K, Omori T, Oikawa K, Kainuma R, Ishida K (2009) Ductility enhancement by boron addition in Co–Al–W high-temperature alloys. Scripta Materialia 61:612–615. https://doi.org/10.1016/j.scriptamat.2009.05.037.
10. Feng G, Li H, Li SS, Sha JB (2012) Effect of Mo additions on microstructure and tensile behavior of a Co–Al–W–Ta–B alloy at room temperature. Scripta Materialia 67:499–502. https://doi.org/10.1016/j.scriptamat.2012.06.013.
11. Knop M, Mulvey P, Ismail F, Radecka A, Rahman KM, Lindley TC, Shollock BA, Hardy MC, Moody MP, Martin TL, Bagot PAJ, Dye D (2014) A new polycrystalline Co-Ni superalloy. JOM 66:2495–2501. https://doi.org/10.1007/s11837-014-1175-9.
12. Meher S, Banerjee R (2014) Partitioning and site occupancy of Ta and Mo in Co-base γ/γ′ alloys studied by atom probe tomography. Intermetallics 49:138–142. https://doi.org/10.1016/j.intermet.2014.01.020.
13. Yan H-Y, Coakley J, Vorontsov VA, Jones NG, Stone HJ, Dye D (2014) Alloying and the micromechanics of Co–Al–W–X quaternary alloys. Materials Science and Engineering: A 613:201–208. https://doi.org/10.1016/j.msea.2014.05.044.
14. Makineni SK, Kumar A, Lenz M, Kontis P, Meiners T, Zenk C, Zaefferer S, Eggeler G, Neumeier S, Spiecker E, Raabe D, Gault B, (2018) On the diffusive phase transformation mechanism assisted by extended dislocations during creep of a single crystal CoNi-based superalloy. Acta Materialia 155:362–371. https://doi.org/10.1016/j.actamat.2018.05.074.
15. Zenk CH, Neumeier S, Stone HJ, Göken M (2014) Mechanical properties and lattice misfit of γ/γ′ strengthened Co-base superalloys in the Co–W–Al–Ti quaternary system. Intermetallics 55:28–39. https://doi.org/10.1016/j.intermet.2014.07.006.
16. Kolb M, Freund LP, Fischer F, Povstugar I, Makineni SK, Gault B, Raabe D, Müller J, Spiecker E, Neumeier S (2018) On the grain boundary strengthening effect of boron in γ/γ′ Cobalt-base superalloys. Acta Materialia 145:247–254 https://doi.org/10.1016/j.actamat.2017.12.020.
17. Xue F, Zhou HJ, Shi QY, Chen XH, Chang H, Wang ML, Feng Q (2015) Creep behavior in a γ′ strengthened Co–Al–W–Ta–Ti single-crystal alloy at 1000° C. Scripta Materialia 97:37–40. https://doi.org/10.1016/j.scriptamat.2014.10.015.
18. Volz N, Zenk CH, Cherukuri R, Kalfhaus T, Weiser M, Makineni SK, Betzing C, Lenz M, Gault B, Fries SG, Schreuer J, Vaßen R, Virtanen S, Raabe D, Spiecker E, Neumeier S, Göken M (2018) Thermophysical and mechanical properties of advanced single crystalline Co-base superalloys. Metall and Mat Trans A 1–11. https://doi.org/10.1007/s11661-018-4705-1.
19. Ismail FB, Vorontsov VA, Lindley TC, Hardy MC, Dye D, (2017) Alloying effects on oxidation mechanisms in polycrystalline Co–Ni base superalloys. Corrosion Science 116:44–52. https://doi.org/10.1016/j.corsci.2016.12.009.
20. Klein L, Shen Y, Killian MS, Virtanen S (2011) Effect of B and Cr on the high temperature oxidation behaviour of novel γ/γ′-strengthened Co-base superalloys. Corrosion Science 53:2713–2720. https://doi.org/10.1016/j.corsci.2011.04.020..
21. Makineni SK, Nithin B, Chattopadhyay K (2015) A new tungsten-free γ–γ' Co–Al–Mo–Nb-based superalloy. Scripta Materialia 98:36–39. https://doi.org/10.1016/j.scriptamat.2014.11.009.
22. Makineni SK, Nithin B, Chattopadhyay K (2015) Synthesis of a new tungsten-free γ–γ′ cobalt-based superalloy by tuning alloying additions. Acta Materialia 85:85–94. https://doi.org/10.1016/j.actamat.2014.11.016.
23. Makineni SK, Samanta A, Rojhirunsakool T, Alam T, Nithin B, Singh AK, Banerjee R, Chattopadhyay K (2015) A new class of high strength high temperature Cobalt based γ–γ′ Co–Mo–Al alloys stabilized with Ta addition. Acta Materialia 97:29–40. https://doi.org/10.1016/j.actamat.2015.06.034.
24. Makineni SK, Nithin B, Palanisamy D, Chattopadhyay K (2016) Phase evolution and crystallography of precipitates during decomposition of new "tungsten-free" Co(Ni)–Mo–Al–Nb γ–γ′ superalloys at elevated temperatures. J Mater Sci 51:7843–7860. https://doi.org/10.1007/s10853-016-0026-1.
25. Murray JL (1982) The Co − Ti (Cobalt − Titanium) system. Bulletin of alloy phase diagrams 3:74. https://doi.org/10.1007/bf02873414.
26. Chen M, Wang C-Y (2009) First-principles investigation of the site preference and alloying effect of Mo, Ta and platinum group metals in (Al, W). Scripta Materialia 60:659–662. https://doi.org/10.1016/j.scriptamat.2008.12.040.
27. Omori T, Oikawa K, Sato J, Ohnuma I, Kattner UR, Kainuma R, Ishida K (2013) Partition behavior of alloying elements and phase transformation temperatures in Co–Al–W-base quaternary systems. Intermetallics 32:274–283. https://doi.org/10.1016/j.intermet.2012.07.033.
28. Nithin B, Samanta A, Makineni SK, Alam T, Pandey P, Singh AK, Banerjee R, Chattopadhyay K (2017) Effect of Cr addition on γ–γ′ cobalt-based Co–Mo–Al–Ta class of superalloys: a combined experimental and computational study. J Mater Sci 52:11036–11047. https://doi.org/10.1007/s10853-017-1159-6.
29. Pandey P, Makineni SK, Samanta A, Sharma A, Das SM, Nithin B, Srivastava C, Singh AK, Raabe D, Gault B, Chattopadhyay K (2019) Elemental site occupancy in the L12 A3B ordered intermetallic phase in Co-based superalloys and its influence on the microstructure. Acta Materialia 163:140–153. https://doi.org/10.1016/j.actamat.2018.09.049.